Title: Characterization of open-cellular polymeric foams using micro-computed tomography

Authors: Cristofaro Timpano[1], Hossein Abdoli[1], Siu Ning Leung[1*], Garrett W. Melenka[1*]

[1] Department of Mechanical Engineering, Lassonde School of Engineering, York University, Toronto, Canada

[*] Corresponding Author: gmelenka@yorku.ca

Graphical Abstract

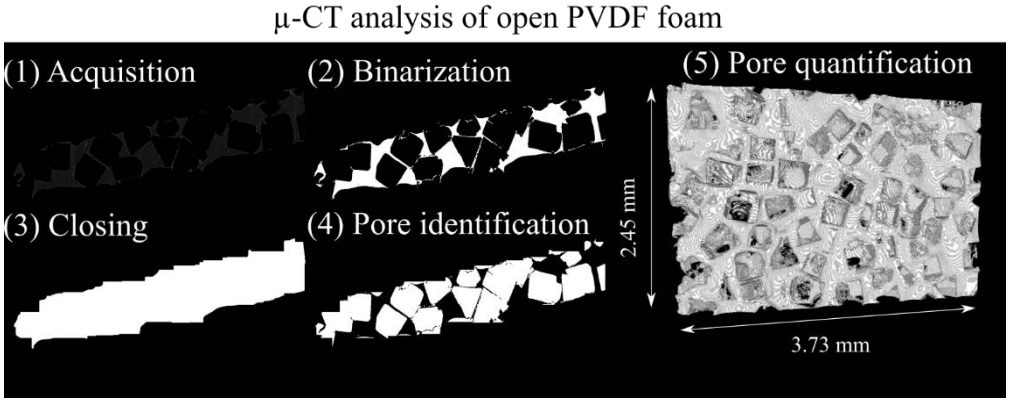

Abstract

Utilization of PVDF (Polyvinylidene fluoride) open-cellular foam allows for the creation of high-efficiency Triboelectric nanogenerators (TENG). The micro-structure of TENG devices can be problematic to characterize accurately using conventional methods like scanning electron microscope (SEM). This work aims to provide a methodology in which representative 3D measurements can be made on open-cellular PVDF foams. Open-cell PVDF foams were produced through a salt-leeching procedure. Analysis of the PVDF foams was done by imaging the sample through a desktop micro-computed tomography (μ-CT) machine to allow for a full 3D dataset to be obtained. Foams were produced with salt sizes of 250-500 μm, 106-250 μm, 53-106 μm, and <53 μm to explore the capabilities of the segmentation procedure at identifying the microstructure of the foam. Images were segmented and analyzed to calculate the porosity, sample volume, pore volume and surface area. Results from μ-CT analysis were compared to that from a SEM, which is currently the most widely used method for assessing open foam PVDF structures. Results from the μ-CT when quantifying pore dimensions proved to be much more representative than SEM due to its ability to capture the entire volume of the foam rather than a single plane. These techniques can be used as the baseline for further verification and improvment the manufacturing of PVDF foam structures.

1.0 Introduction

Triboelectric nanogenerators (TENG) are used to harvest wasted mechanical energy and convert it into electricity. The efficiency of TENG is highly influenced by two significant factors: the material and the microstructure of the porous friction layer. Materials with a high triboelectric effect and electrostatic induction facilitate the best transfer between mechanical energy to electrical energy [1]. Once a material is selected to improve output further, it is recommended for it to have a high surface area to volume ratio to provide room for the accumulation of a triboelectric charge. Lee *et al.* revealed that utilizing a porous friction layer with cell sizes on the micrometer to nanometer scale is an effective method for increasing surface area and, thus, the throughput of these devices [2].

Polyvinylidene fluoride (PVDF) is an ideal material for TENG devices as it is inexpensive, environmentally benign, non-toxic and has a natural dipole moment [1]. PVDF is a semi-crystalline polymeric material that exhibits pyroelectric, piezoelectric, and triboelectric properties and has high thermal, chemical, and oxidative stability [3]–[5]. By fabricating PVDF into an open cellular foam structure, it is possible to significantly increase the surface area to volume ratio of samples comparing to a nonporous film, which positively affects the triboelectric properties of PVDF. However, a major challenge faced when doing so is in the characterization of these individual pores due to their high degree of connectivity in the open cellular foam.

Currently, the most utilized method for characterizing the cell structure is with a scanning electron microscope (SEM) [6], [7]. While this method is widely utilized, there are several disadvantages to this approach. One of the major drawbacks is that it requires the destruction of the sample to capture a single cross-sectional image of the micro-structure. Additionally, when utilized to image the cross-section of a non-metallic material, such as a polymer, it must be coated by a conductive material, typically gold, which can be expensive. Most importantly though is the technique only provides a single 2D image, which is unrepresentative of the true pore structure.

High-resolution micro-computed tomography (µ-CT) non-destructively enables the acquisition of full 3D images of a materials micro-structure with minor sample preparation. Therefore, µ-CT is an ideal technique for characterizing polymeric open cellular foams [2]. µ-CT uses radiographic imaging in which x-rays are passed through a sample material [8]. The attenuation of the beams is identified by measuring the x-ray intensity as they propagate through the sample [8]. Principally, the attenuation is proportional to the density of the material but can also be affected by the sample composition [8]. This knowledge allows the creation of a series of high-resolution cross-sections of an object's internal structure [8]. By performing this technique at multiple angles, one can effectively triangulate the positions of the features in 3D space. These cross-sectional images can then be combined to create a volumetric representation of the object in the µ-CT field of view (FOV). The ability to use these scans to resolve features on a micro-scale allows improved flexibility to characterize a material's internal structure precisely. Also, µ-CT has the flexibility to characterize samples prepared with different materials since varying object densities can be resolved in the images as different intensity greyscale values. The µ-CT process allows for distinct visualization of different materials as well as any cracks, voids, or defects in these materials to not only be visualized but also properly located and measured [9], [10].

Due to the advantages of µ-CT, researchers have begun to use this method to examine a variety of different traditional and non-traditional materials. Cnudde *et al*. previously investigated the application of µ-CT to create pore size distribution curves and identify micro-cracks or air bubbles within the samples of concrete and building stones. This same process applied the technique to sandstone [11], [12]. Scans of the sandstone were taken at a resolution of 7.4 µm, and an overall porosity of 18% was found. It was noted that pores below the size of the scan resolution were not computed. In another work, Skarżyński *et al*. investigated concrete further by loading the sample in a quasi-static three-point bend test and measured cracks along the width of the material via µ-CT [13]. Also, building stone metal powders were investigated by Cai *et al.* [14]. Porosity for four different laser sintered samples was measured by using an image processing software (Fiji) to calculate fraction area. However, this study only included pore sizes larger than 74 µm. There was a negligible difference between theoretical and experimental porosity. These studies demonstrate the effectiveness of the µ-CT technique to measure the internal porosity of structures.

Beyond traditional materials, researchers have used µ-CT to analyze various composite and polymeric materials such as carbon fibre-reinforced composite (CFRC), laminates, braided composite materials and polymer structures [15]–[18]. Little *et al.* showed that there was no significant error when using µ-CT to quantify the three-dimensional size, shape, and pore distribution of voids in CFRC laminates [16]. This study supports the practicality of this technique to quantify the material properties for non-traditional materials accurately. Recently, some efforts have made to examine the utilization of µ-CT on braided composite materials. The µ-CT method allows examination of the void content along with properties of the mesostructured of the material such as yarn size, spacing, thickness, and direction [15], [17], [18].

While the utilization of µ-CT has proved effective at measuring the porosity of samples, its usage on porous PVDF sample has yet to be tested. Additionally, the salt leaching technique used to create TENG produces an extensive open cellular network. Such a pore network provides a unique challenge in segmentation and analysis because of the high degree of connectivity between the salt produced pores. This study aims to describe a technique that allows for the investigation and verification of the manufacturing of open-cellular foam structure. Specifically, this study is aimed at investigating a PVDF foam and studying its porosity and surface area. Four different microcellular PVDF foams were fabricated for this study. A simple salt leaching process was used to manufacture PVDF open cell structure with varying ranges of pore size (*i.e.*, 250-500, 106-250, 53-106, and <53µm). Fabrication of triboelectric nanogenerators is supported by accurate quantification of surface area and porosity. Also, porosity and surface area measurements will allow us to quantify any inconsistencies in manufacturing. The method suggests a simple technique to find the total porosity and surface area of a sample using digital image processing software.

2.0 Methodology

2.1 Sample preparation

PVDF open-cell foams were prepared using a salt leaching process and compression molding machine (Craver Press, 4386 CH). PVDF powder (Kynar 741, Arkema) was used as base material and). Also, commercial salt particles were sieved into four different sizes (*i.e.*, 250-500, 106-250, 53-106, and <53µm). The following procedure was used for the foam fabrication. First, a mixture

of 20 wt.% PVDF powder and 80 wt.% salt were dry-blended and loaded into molds with a diameter of 2 cm and thickness of 0.5 mm. Second, the mold was loaded into a compression molding machine preheated to a temperature of 185 ℃. Third, the mold was equilibrated at the preset temperature. Fourth, the mold was cured under compression molding machine at 185 ℃, for 5 minutes by applying a negligible pressure. Next, the compression molding pressure ramped up to 27 MPa and mold was kept at the same temperature for another 5 minutes. The mold and samples were taken out and cooled by cooling plates for 5 minutes. Samples were submerged into water for 72 hours to leach out the salt particles from structure and water replaced every day with fresh water to avoid saturation. Finally, all the PVDF open foam samples were dried overnight in a vacuumed oven at 60 ℃.

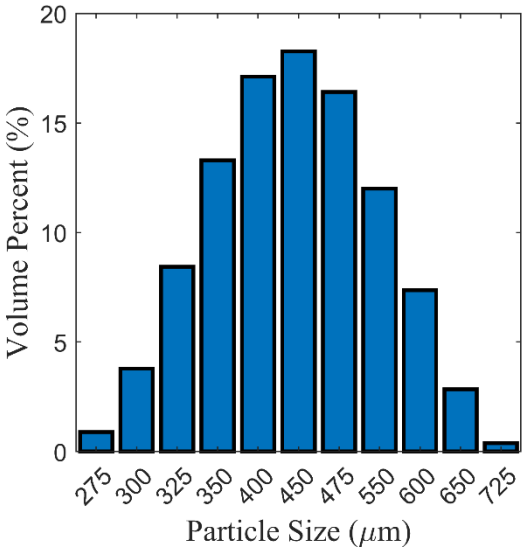

Figure 1: Contribution of salts to total volume measured after sieving salts from the sample.

2.2 Process Flow

A three-part process was utilized to characterize the size and distribution of pores in the open-cellular foam. Figure 2 outlines the key steps used in this study to characterize the pore structure of the PVDF, which will be discussed in greater detail in the following sections. The first step toward characterizing the pore structure of the foam is to obtain a three-dimensional dataset that was done via μ-CT. A series of post-processing procedures was then conducted to allow for representative measurements of the pore structure. After processing the data, the digital analysis could then be conducted to allow for the pore size, distribution, and pore surface area to be measured.

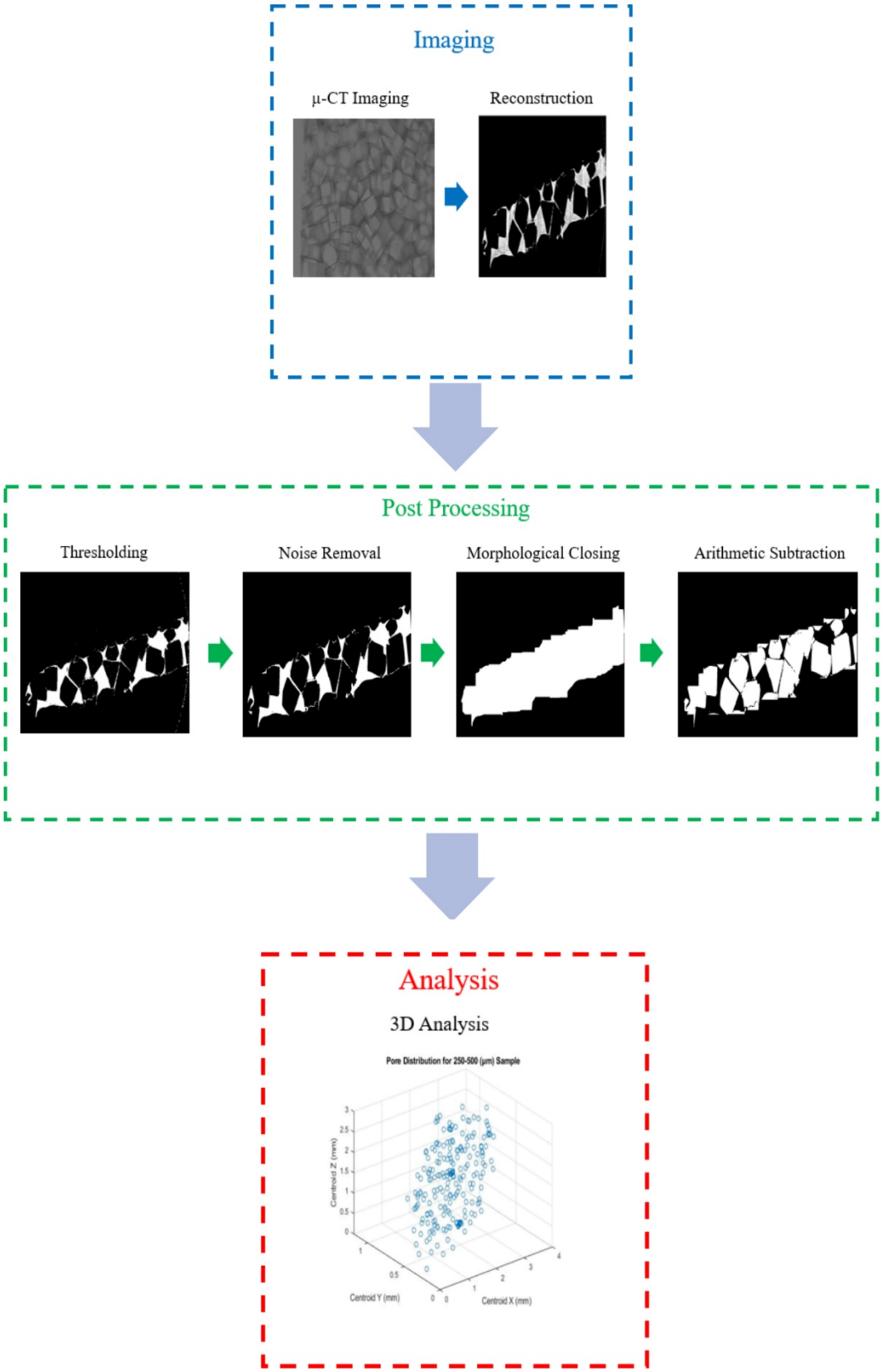
Imaging
μ-CT Imaging
Reconstruction
Post Processing
Thresholding
Noise Removal
Morphological Closing
Arithmetic Subtraction
Analysis
3D Analysis
Pore Distribution for 250-500 (μm) Sample
Centroid Z (mm)
Centroid Y (mm)
Centroid X (mm)

Figure 2: Computed tomography acquisition and analysis process utilized to characterize the pore size and distribution of the PVDF foam. Three main steps are involved: imaging to collect sample data, image processing to identify pore geometry, and analysis to quantify the pore structure.

2.3 Computed Tomography Image Acquisition

All µ-CT scans were performed using a desktop µ-CT (Skyscan 1272, Bruker-MicroCT, Kontich, Belgium) machine. Samples were cut into square-shapes with a side length of 5.73 mm. A 6.45 mm diameter cylindrical holder was used to mount the PVDF samples inside the µ-CT machine. The bigger size of the holder allowed for an air gap to be maintained in the scanner field of view. Moreover, the air gap positively affects contrast. At the same time, it aids in maintaining the sample in the scanners field of view (FOV), and thus avoid any truncation in data from the sample leaving the FOV.

The scanner was set for a voxel size of 0.8 µm with an image resolution of 4904x3280 pixels. The 0.8 µm voxel size was chosen to resolve the smallest pores in the image, which were expected to have a size of less than 53 µm. The sampling voltage and current were 30 kV and 200 mA, respectively. The sampling source voltage and current were selected to ensure optimal contrast as PVDF is a low-density polymer. Due to the low density of the PVDF polymer, no filter was required during scanning. Finally, due to the high frequency of pores, especially at the smaller salt sizes, a rotation step of 0.1° was chosen to ensure proper resolution of the complex pores network.

2.4 Reconstruction

Once the µ-CT scan was completed, the shadow projections were converted into cross-sectional images through using a reconstruction software package (NRecon version 1.7.1.0, Bruker-MicroCT, Kontich, Belgium) and reconstruction engine (InstaRecon version 2.0.3.7, Bruker-MicroCT, Kontich, Belgium). A reconstructed set of single cross-sectional images can be seen in Figure 3. In Figure 3, sample images of the 250-500 µm, 106-250 µm, 53-106 µm, and <53 µm PVDF foams are shown. These images demonstrate that sample morphology can be analyzed using the µ-CT method. Moreover, Figure 3 confirms that this method can be used for high quality and accurate digital measurements with minimal interference from noise and ring artifacts. It is important to note that the minimal noise that is seen here is due to enhancing the contrast to aid in the visualization. For the samples with a pore range of 106-250 µm, a negligible amount of beam hardening was observed; however, it was mitigated using post-processing techniques.

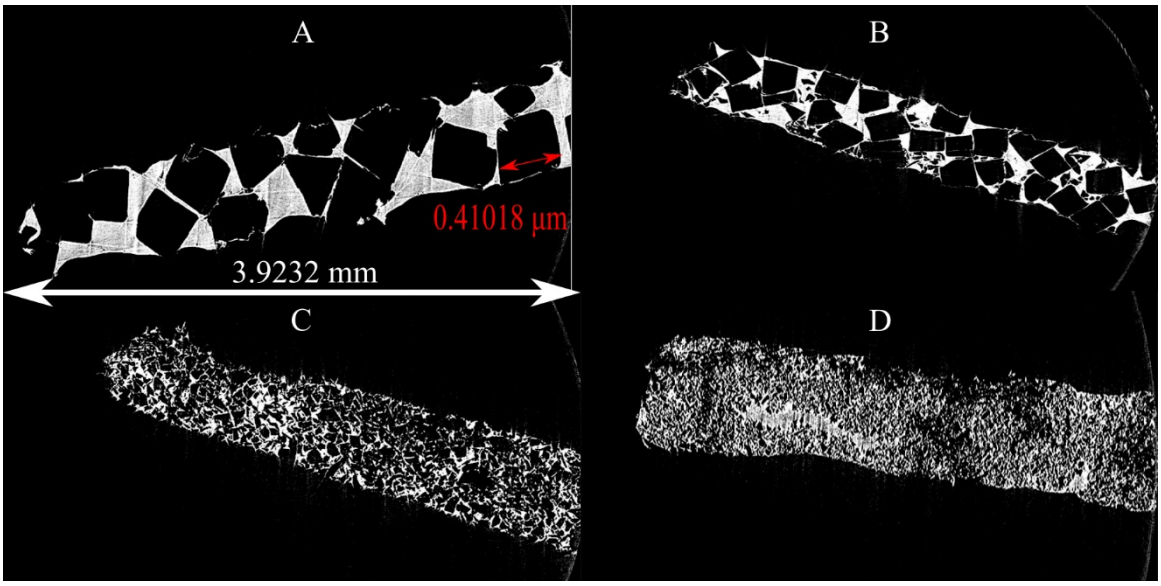

Figure 3: Contrast-enhanced greyscale cross-section images for the four PVDF samples with pore size: A) 250-500 µm, B) 106-250 µm, C) 53-106 µm, and D) <53 µm.

2.5 Post Processing

An image processing software package (CTan version 1.16.8.0, Bruker µCT, Belgium) was used for the post-processing of PVDF samples. CTan requires 8-bit images before performing measurements on the images. A three-step procedure for sample examination was followed, consisting of (1) thresholding to binarize the image, (2) despeckling to remove noise, and (3) image erosion to eliminate processing artifacts. The specific parameters for image processing operations are shown in *Table 1*. Thresholding limits for different samples were defined in a way to make the pores and polymer medium distinguishable. Optimal thresholding ranges for the samples was performed by keeping the upper greyscale limit at 255 and adjusting the lower threshold limit to 11, 16, 12, and 14 for 250-500 µm, 106-250 µm, 53-106 µm, and <53 µm pore sizes ranges, respectively. The chosen threshold limits are based on the greyscale histograms seen in Figure 3, which show the highest count of greyscale values is beneath these greyscale values. After thresholding, those greyscale particles which were not associated with the background were converted to binary. Figure 5 displays the result of binarized images where the white colours represent the PVDF polymer. The binarized images also show the created noise from the scanning process. This noise is an inherent part of the scan, and its intensity is strongly affected by the scanning parameters. This noise can be removed digitally by using a despeckling operation. Despeckling eliminates unwanted random black or white pixels, which are below a user-selected pixel size. A square kernel size was chosen for this operation as it provided the best reduction in noise without removing PVDF pixels. The final thresholded images for all four samples are shown in Figure 6. It can be seen that the thresholding and noise reduction results in a clear interface between the polymer and the pore network for all four pore sizes and prepare them for digital analysis. By examining the four images, one can observe that there is a significant change in the morphology of the microstructure between the samples. As the pore sizes begin to get smaller, the networks in the cell walls start to become larger and more abundant. The smaller pores have

respectively smaller walls, which are structurally weaker. Additionally, it can be seen there is a significant accumulation of polymer that has formed in the <53 µm sample.

Table 1: Digital image processing techniques used to transform greyscale images

Pore Size (µm)	Thresholding Lower Limit	Thresholding Upper Limit	Despeckling (White Pixels)	Despeckling (Black Pixels)	Erosion (Pixels)
250-500	11	255	20	8	4 (Square Kernel)
106-250	16	255	20	3	5 (Square Kernel)
53-106	12	255	3	n/a	1 (Hexagonal Kernel)
<53	14	255	15	20	1 (Hexagonal Kernel)

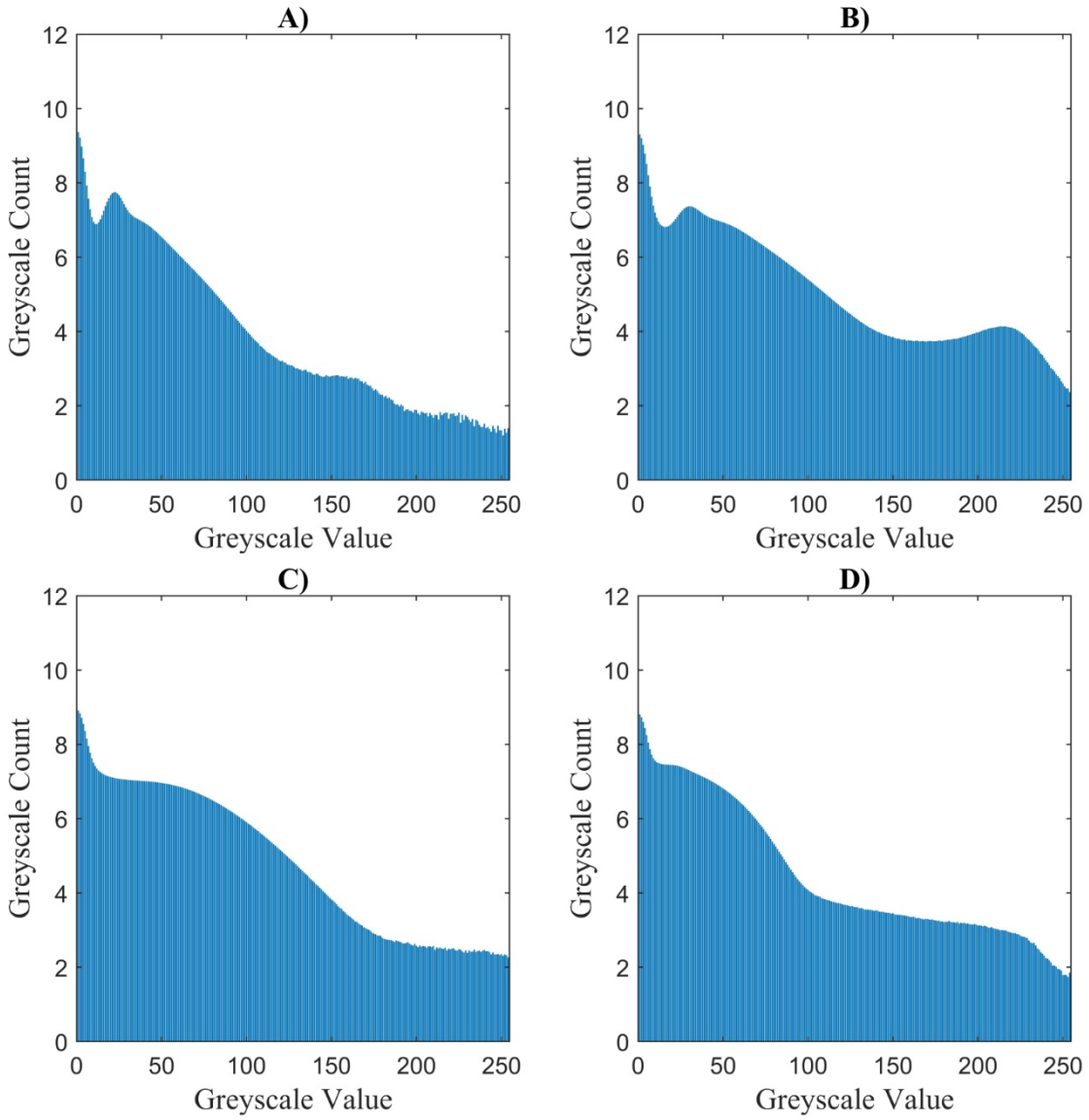

Figure 4: Log scale greyscale histogram for the four PVDF samples. (A) 250-500 µm (B) 106-250 µm (C) 53-106 µm and (D) <53 µm.

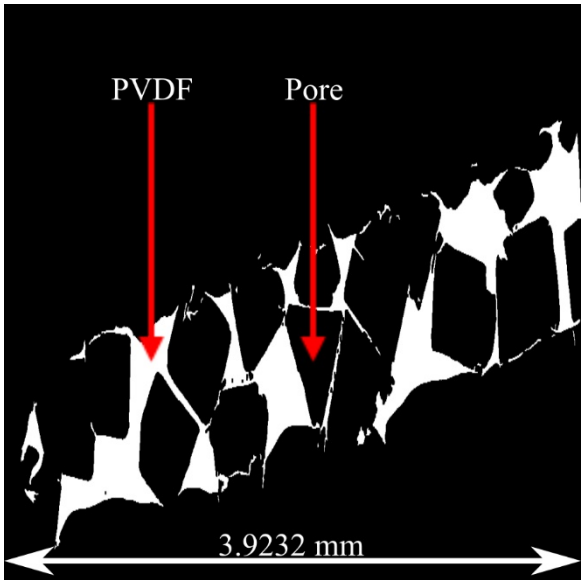

Figure 5: Binarized PVDF sample indicating the polymer and pore content of a cross-section of the 250-500 µm sample

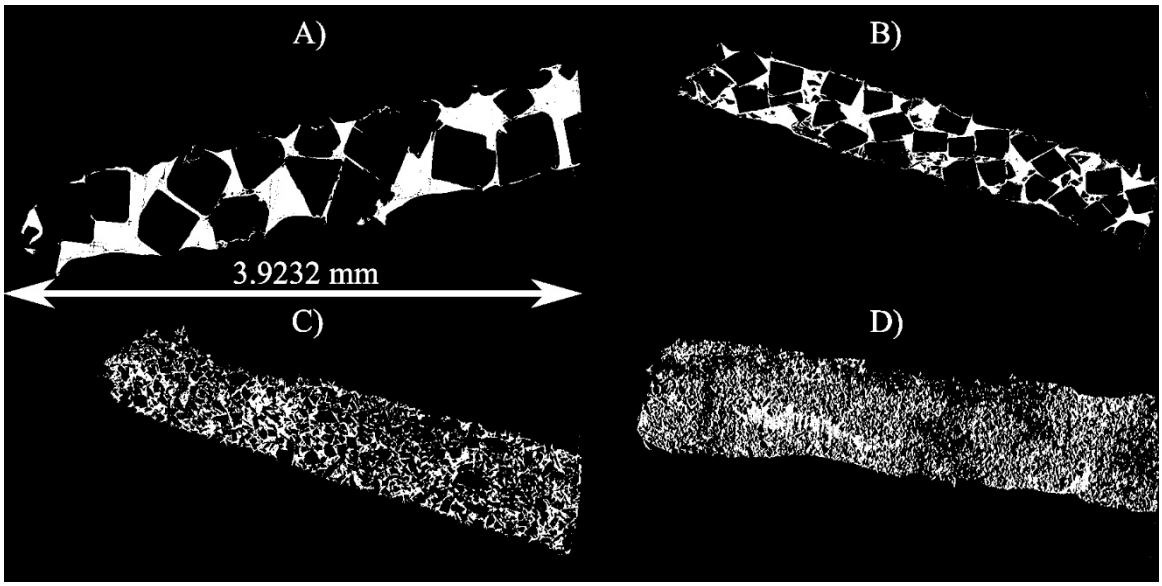

Figure 6: 8-Bit thresholded and despeckled cross sections for the four PVDF samples: A) 250-500 µm, B) 106-250 µm, C) 53-106 µm and D) <53 µm.

The total volume of the samples was found by filling the binarized and despeckled. The first step to fill the pores was using the remove pores operation. The remove pores operation scans the image for all closed pores, which is defined as black pixels surrounded by white pixels and then

fills them with white pixels. The presence of these closed pores within the sample was notably small as the samples were prepared to contain only open pores, but this process ensures that no embedded voids are filled. A morphological closing operation was performed on the images to close the bulk of the pores (open pores). The morphological closing is that it first applies a dilation and then an erosion. The dilation operation fills black pixels through the expansion of all white pixels by the designated kernel size. As a result of this, the total volume of the sample increases. For the volume to become more representative of the actual sample volume, the closing operation follows the dilation with erosion by removing white pixels at the edge of the sample. The kernel size for this operation was chosen based on the estimation of the largest pore to ensure all pores within the sample fill in from the morphological closing, which is seen in Table 2.

A consequence of using this kernel size is that smaller pores will be increased in size. Even though the erosion operation does compensate for the size increase, there is still a slight increase in total volume due to the kernel size selection. Thus, a single-pixel kernel size erosion was used to bring the volume down to its correct size.

Table 2: Image processing kernel sizes used in the morphological closing operation to digitally fill in pores.

Pore Size (μm)	Morphological Closing Kernel Size (Pixels)
250-500	50
106-250	40
53-106	20
<53	15

The bitmaps were then saved, and the volume and surface area of the samples were computed. The “3D analysis” function in CTan operates by locating a corresponding section of 1 in the image matrix, which is represented by white voxels within the image. The white voxel within the volume of interest (VOI) converted to a dimensional unit through a conversion factor based on the scan parameters. Similarly, the surface area can be calculated by analyzing the voxels for only white pixels bordered by black pixels.

After processing of both the porous structure and the filled structure, identification of the open cells could be performed. The open cellular structure pores were filled in by utilizing the same method that was previously outlined above. A bitwise operation was then performed to create a copy of the region of interest of the filled-in structure. The porous PVDF image stack was then reloaded, and by using a subtraction arithmetic operation, the difference of the filled-in image and the porous structure image was taken, allowing for a view of the open pore network to be acquired. In the next step, the bitmaps were saved, and a 3D analysis was completed to get the open pore volume and surface area. This process is outlined in Figure 7 for the 250–500 μm sample. Figure 7 (A) shows the greyscale image of the PVDF from the reconstruction process. The binarized image of the cross-section is then shown in Figure 7 (B), and its correspond full volume is shown

in Figure 7 (C). Finally, Figure 7 (D) shows the pore network of the structure visualized as white pixels, which is the exact inverse of Figure 7 (B).

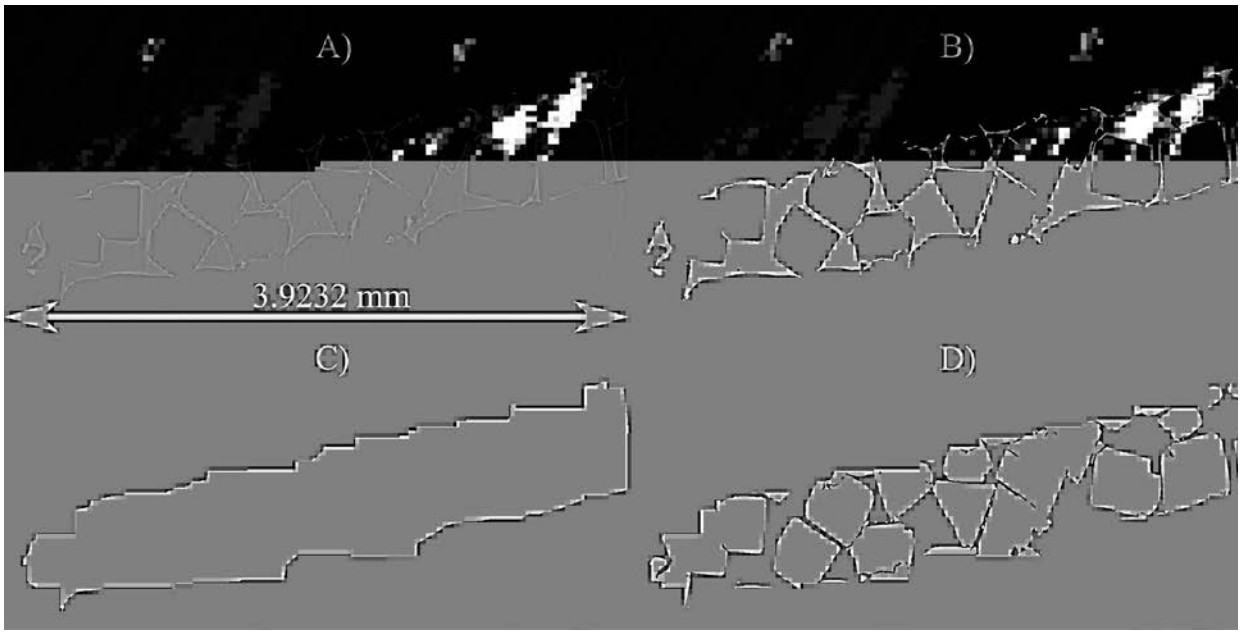

Figure 7: Total volume and pore volume identification process for 250-500 µm sample: A) greyscale image of the PVDF, B) PVDF structure after binarization, C) Filled in PVDF sample D) Open Pore Network

2.6 Visualization of the 3D Pore Structure

While cross-sectional images allow for digital analysis, it is often beneficial to reconstruct them into a 3D model. The advantage of a 3D model is that one can visually inspect the morphology of the sample from different angles. The 3D model allows for a full investigation of porous polymeric structures, while their visualization from cross-sectional images is difficult. 3D reconstruction was completed by using Fiji (Fiji, National Institutes of Health, Bethesda, MD). The binarized bitmaps from the previous step were uploaded as an image stack to Fiji. The "3D analyzer" plugin was used to create the 3D models of the PVDF samples. The 3D models of the four samples are shown in Figure 8. The polymer is shown as the white interconnected materials, while the pore network is the space in between.

2.7 Quantification of the Salt Size Distribution

Digital analysis was performed to quantify the distribution of salt sizes used in the sample fabrication process. Due to the necessity for the salts to be leached out, a connected network needed to be formed between cells. This connected network requires segmentation to separate the pores, and their sizes may be individually measured. An erosion procedure was performed with the pixel sizes to separate the pores, which are presented in Table 3. Two significant factors dictate how the erosion procedure was performed. The first factor is the degree of connectivity between the pores as the higher the connectivity, the large the erosion needs to be to separate them. Furthermore, if the pores are significantly connected, it is impossible to separate them from each other by erosion processing. The second factor is the size of the pores. By performing an erosion procedure, we are

making a trade-off between reducing the pore size but getting a better definition of the pores. Thus, if the pores are already small, it becomes challenging to separate the pores without completely removing them. The kernels shape and pixel sizes depicted in Table 3 were found to offer the best compromise between pore separation and size reduction.

Table 3: Erosion procedures performed to separate pores from the image for pore size identification.

Sample	Erosion (Pixels)	Kernel Shape
250-500 µm	8	Square
106-250 µm	7	Square
53-106 µm	3	Hexagonal

3.0 Results and Discussion

3.1 Total Porosity

Prior work by Chu *et al.* has shown that the ratio of salt size has minimal effects on porosity, and the major contributor is the polymer to salt ratio [19]. For the samples produced in this study, the salt to polymer ratio was maintained between 30 and 70 wt% for all salt sizes, and thus it is expected that the porosity should remain around 70% for all four samples. The CT analysis of these samples showed that after a decrease in salt size from 250-500 µm to 106-250 µm increased porosity. There is a subsequent decrease in porosity as the pore sizes continue to decrease. However, there is not a significant difference between the porosity of these samples as they all are around 60-70%. The results are all outlined in Table 4. These results are consistent with results presented by Ghosh *et al.* in which porous scaffolds made from 70% Polylactic acid and 30 % corn starch (SPLA70) through compression molding of salts were analyzed for porosity via computed tomography [20]. It was found that samples made with an 80:20 wt% (salt: polymer), but different salt sizes had a porosity ranging from 77.9-80.2%, while theoretically, their porosity should remain constant. The resultant percent difference achieved by Ghosh *et al*. was between 0.25-2.625%, which is comparable with that obtained for the first three samples in this study 1.028-3.557%. Low error was achieved for the 106-250 and 53-106 µm, which contain smaller pores than what was previously studied by Ghosh *et al*.. The variation in porosity for the 250-500 µm 106-250 µm and 53-106 µm PVDF samples is in good agreement with what has been previously presented by Ghosh *et al.* and can be considered merely as a result of different salt sizes and employed digital processing techniques. However, the <53 µm sample still had a porosity in the range of 60-70%, it is different enough to be considered for further investigation since its porosity value cannot be attributed merely to a difference in salt size. The manufacturing of these samples and their 3D models help to explain the variation of the porosity <53 µm sample.

Table 4: Comparison of sample volume, pore size and porosity for the PVDF samples examined using CTan.

Pore Size (μm)	Total Volume (mm^3)	Pore Volume (mm^3)	Porosity (%)
250-500	4.674	3.179	68.01
106-250	4.059	2.813	69.28
53-106	4.144	2.798	67.51
<53	4.020	2.427	60.38

While there is not a significant difference in porosity between the samples, the difference that is observed is a consequence of the manufacturing of these samples, especially with the <53 μm sample. The small salt size of the <53 μm sample was susceptible to bundling together before the compression molding process, which was used to make PVDF samples in this work. The bundling of these salt particles could lead to uneven distribution of pores throughout the sample, which leads to a reduction in overall porosity. Also, as the salt size decreases, the accumulation and higher packing efficiency of particles might affect the actual porosity. In Figure 8, the 3D models of the PVDF are shown for different pores sizes of PVDF samples. For the smaller pore size (*i.e.*, <53 μm sample), there is an uneven distribution of PVDF into the structure, which has left regions within the sample with an agglomerated polymer. The unequal distribution of PVDF can also be seen in the 2D cross-section in Figure 9, where there is a defined region of densely packed polymer without pores.

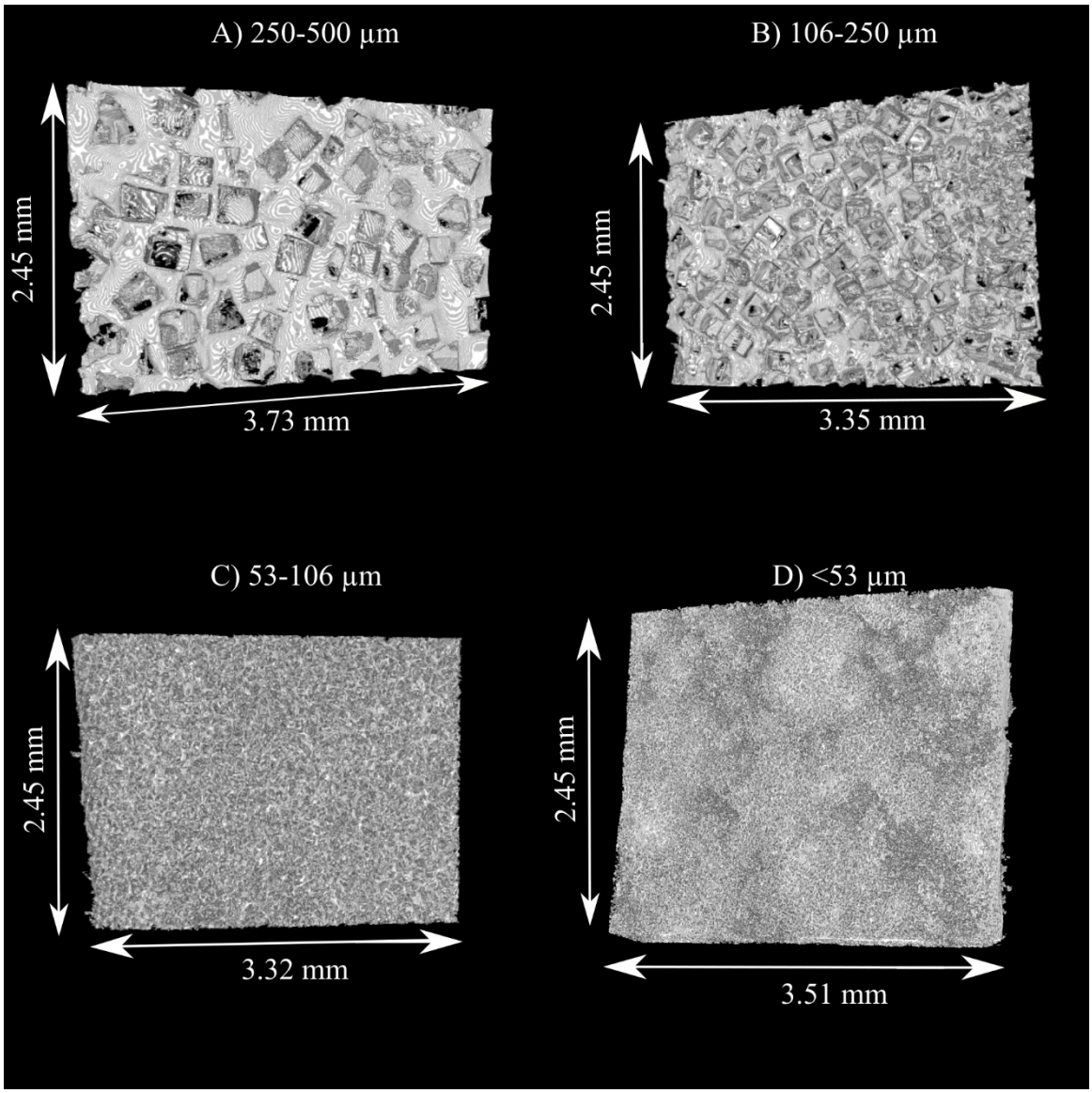

Figure 8: Three-dimensional image of the four samples of microcellular PVDF foam samples. A) 250-500 µm pore range, B) 106-250 µm pore range, C) 53-106 µm pore range, and D)53 µm pore range. Grey indicates the PVDF polymer, while the black is considered empty space left from the salt leaching

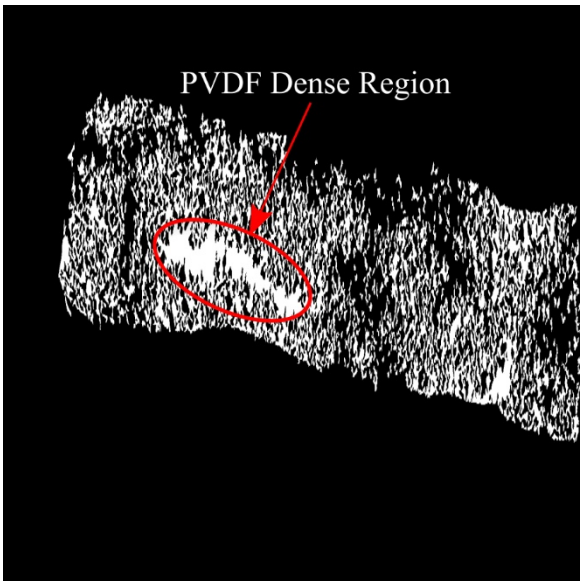

Figure 9: Cross-section of the <53 μm PVDF sample with a region of highly dense polymer

3.2 Pore Size Distribution

Quantification of the individual pore sizes for the foams proved challenging due to the interconnected pore structure of the foam formed from the salt leaching procedure. Segmentation of the pore volumes within the sample showed the presence of a single large pore within each structure and then a series of smaller pores. This single large pore contributed to more than 98% of the total pore volume. The 3D models shown in Figure 8 shows the reason behind this is because the pores in the samples are all interconnected. The interconnected pore network is a result of the leaching process, where a strongly connected network is necessary to allow for salts to be leached out.

The distribution of the individual salts within the sample was determined after image processing to identify individual pores. An erosion process was applied to separate the individual salt pores from the pore network. This erosion process was dependant on the amount of interconnectivity between the salt pores. The salt sizes were estimated by assuming that they have a cubic shape. Figure 10 displays the size distribution of salt particles within the polymeric structure. Due to the significant accumulation of PVDF and salts in the <53 μm sample, its salt particle size distribution was not analyzed since pores could not be distinguished for further analysis. Figure 10 shows that 53.45 %, 98.16 %, and 57.58 % of the pores fall within the range of 250-500 μm, 106-250 μm, and 53-106 μm, respectively.

The image processing procedure used in this work to separate pores can result in an underrepresentation of the actual pore size. Pore underrepresentation is evident from the volume distributions for the 250-500 μm and 106-250 μm samples, where the upper limit of the ideal salt size cannot be seen in the digital images. However, the small kernel sizes used in the pore segmentation procedure does not significantly reduce the size of the pores. Therefore, the majority of pores are measured within to be within the range of their constituent salt sizes.

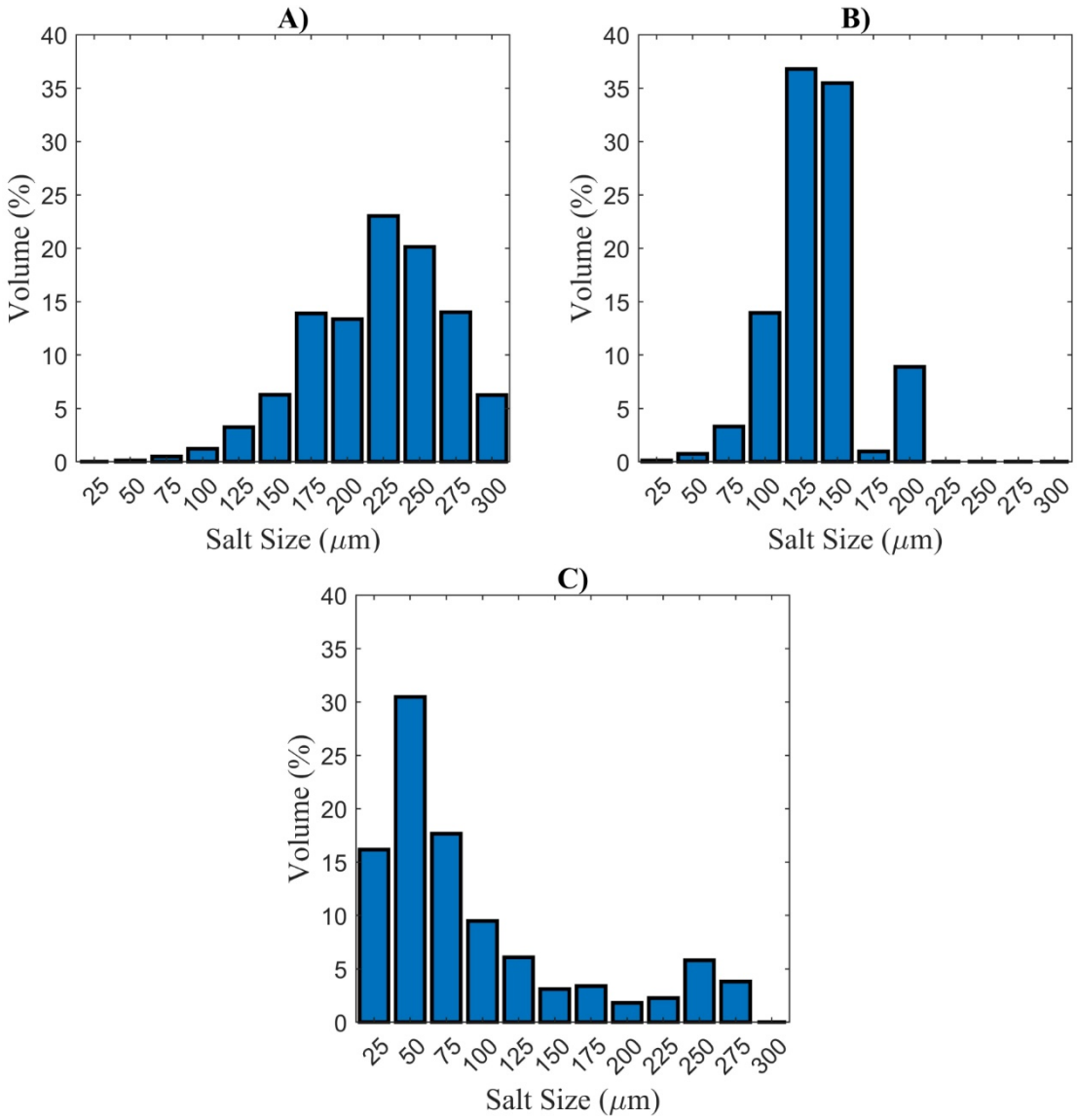

Figure 10: Contribution of different sizes of salts to the total pore volume. A) 250-500 µm salts, B) 106-250 µm salts C) 53-106 µm

For the 53-106 µm sample, some salts appear above the expected range of salt sizes. It is expected that the erosion of the example should reduce the size of the pores. The presence of large pores that remain after the erosion procedure must be attributed to the overlapping of salts together before the leaching process and thus acts as a single pore. Pore overlap would prevent the erosion process from separating the respective salt-induced voids. For further analysis, the centroids of all the salts within the sample for the three different samples were plotted in Cartesian coordinates in Figure 11. There is a distance between the pore centroids for the 250-500 µm and 106-250 µm samples. Figure 11 shows that the erosion procedure has actively separated the majority of the individual salts from the cell network. However, examining the plot for the 53-106 µm reveals a significant overlap in the centroids. The examination of the pore centroid locations implies that the associated pores in the original image are close together. Consequently, increasing the

likelihood that the pores are so significantly overlapped makes it challenging to separate them properly.

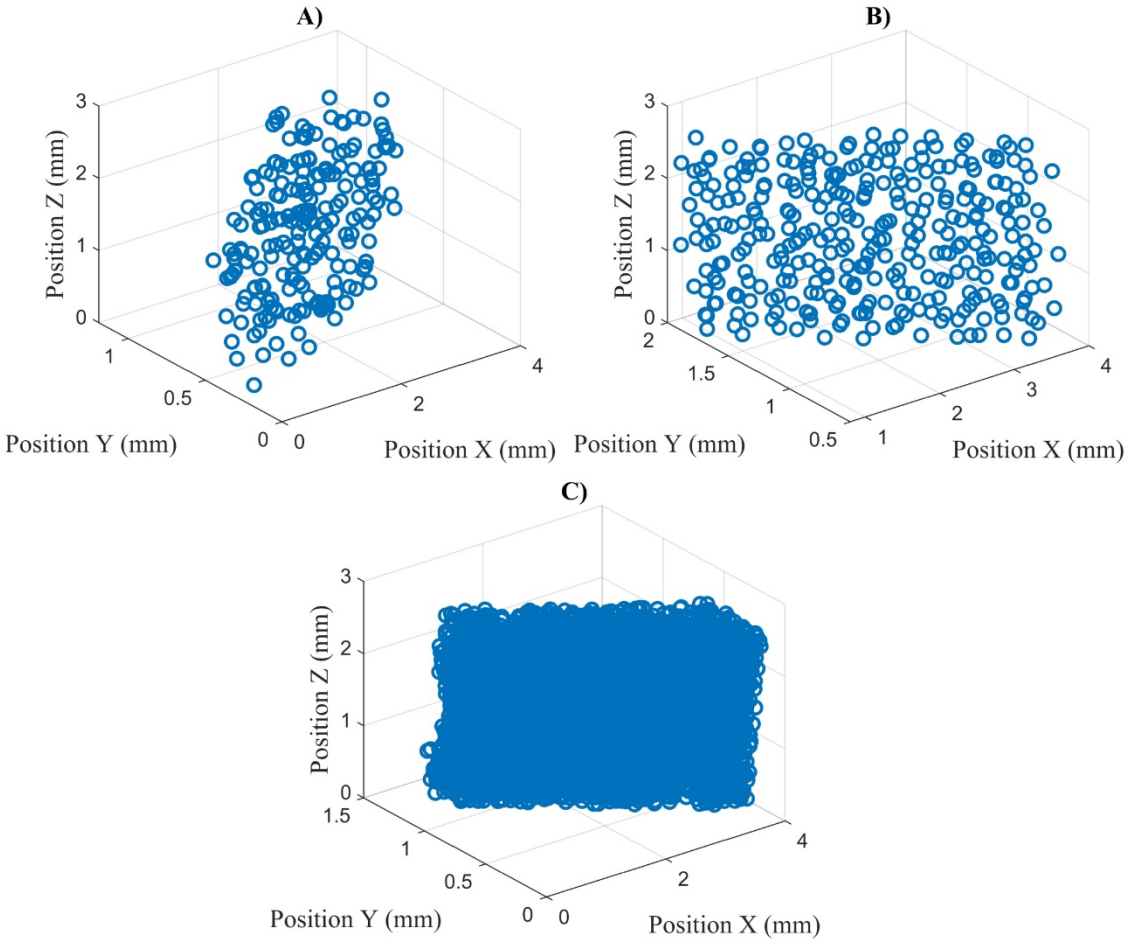

Figure 11: Distribution of open-cell centroids for the: A) 250-500 µm PVDF sample B) 106-250 µm PVDF sample, and C) 53-106 µm sample.

Also, cross-sectional SEM micrographs in Figure 12 show the pore structure of PVDF open-cell samples fabricated with different salt size after salt leaching. The point here is that beside special preparation requirements for SEM, such as gold coating and cryo-fracturing, the SEM process only provides information on one cross-section. At the same time, µCT-scan provides morphological information for all structures without resulting in the sample damage.

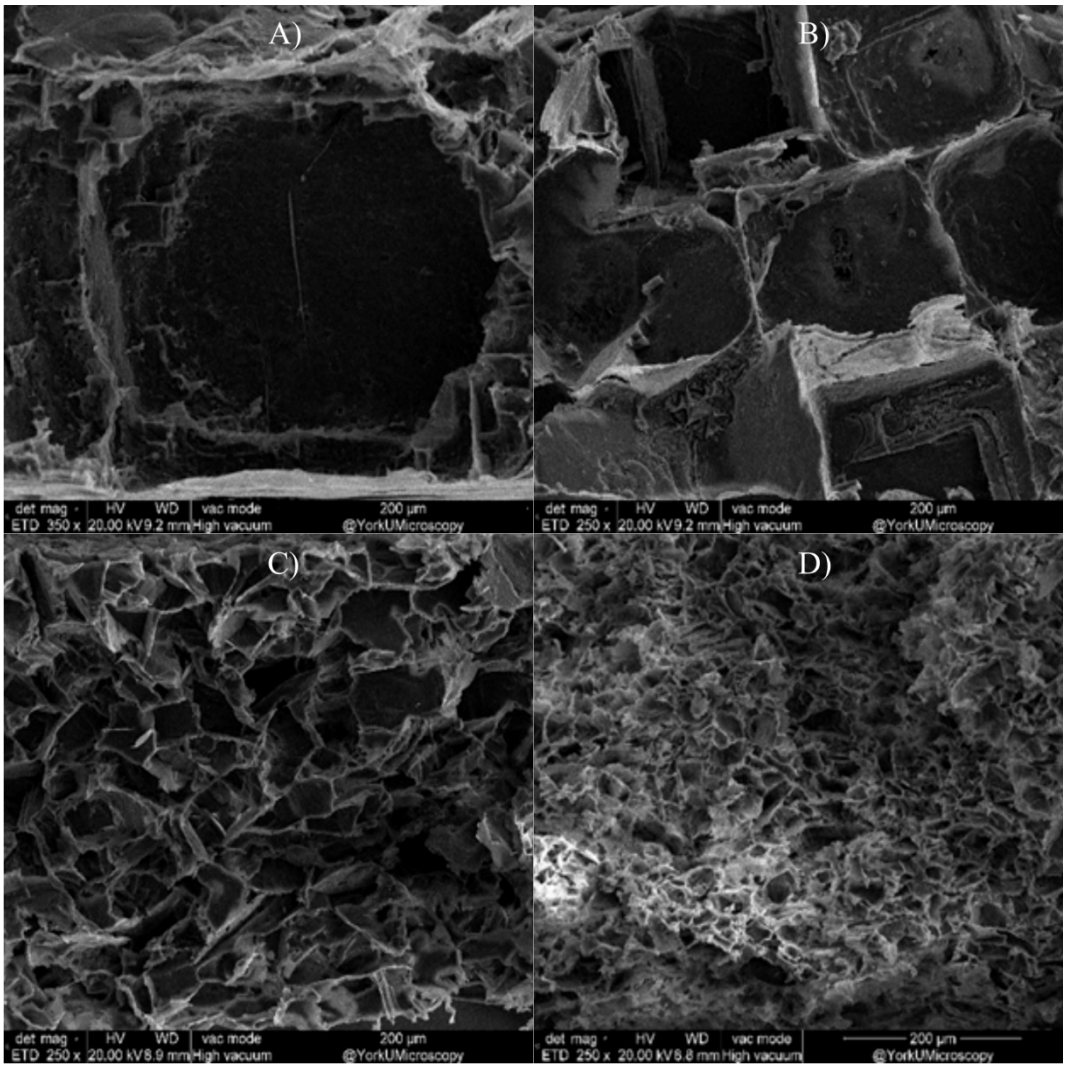

Figure 12: Cross-section SEM micrographs of PVDF open-cell structures after salt leaching process fabricated with salt particles with a size of a) 250-500 µm, b) 106-250 µm, (c) 53-106 µm and d) less than 53 µm.

Table 5 shows the average pore size for the PVDF sample that has been measured using Fiji/ImageJ. The SEM results display a high level of inaccuracy, which is indicative of the average diameters that are much smaller than their respective salt size and high standard deviation. The inaccuracies seen are due to the nature of SEM imaging when compared with µ-CT. Figure 13 (A) shows the ideal case for SEM. For SEM to provide an accurate measure of pore size, the plane of the fracture surface must contain the entire cross-section of the pore. In actuality, the fracture surface looks more like what is shown in Figure 13 (B), where due to the 3-Dimensionality of the pore-network, different geometry can be observed in anyone one 2D plane. This issue is circumvented by utilizing µ-CT, which allows for the characterization of the whole microstructure of the sample.

Table 5: Cell diameters and standard deviations of open-cell PVDF using SEM images

Sample Type	Average of pores diameter (µm)	Standard Deviation (µm)
Open-cell after salt leaching (salt size less than 53 µm)	4.7	3.9
Open-cell after salt leaching (salt size 53-106 µm)	16.37	12.2
Open-cell after salt leaching (salt size 106-250 µm)	43.68	68.5
Open-cell after salt leaching (salt size 250-500 µm)	69.97	104.3

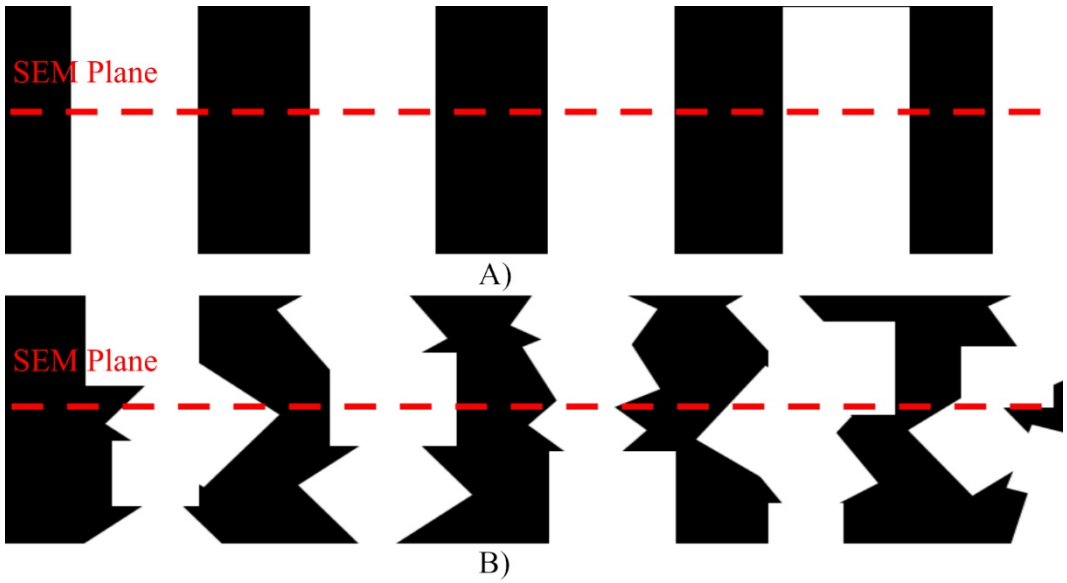

Figure 13: Symbolic representation of open cellular PVDF foam: A) Ideal case for SEM imaging and B) actual pore geometry for SEM imaging.

3.3 Pore Network Surface Area

Previous research shows that as the size of salt particles and, as a result, the pore sizes of foam structure decreased, the surface area will increase [21]. Results from the CTan software confirmed this trend while they showed a nonlinear increase as the pore sizes decrease, which can be seen in Figure 14. It is important to note that the total volume of the sample can have a substantial effect on the open cell surface area since the larger porous sample possesses a higher surface area. Here,

the impact of volume on the surface area was removed by choosing the same volume of porous PVDF samples (*i.e.*, 0.5 mm^3) for analysis.

Samples prepared with a salt particle size of less than 53 μm had higher surface area compared to the rest of the samples, which is because of their smaller pore sizes. These trends agree with what has been seen in previous literature and display the ability of CT analysis and digital image promising to predict the surface area of different features within the material microstructure.

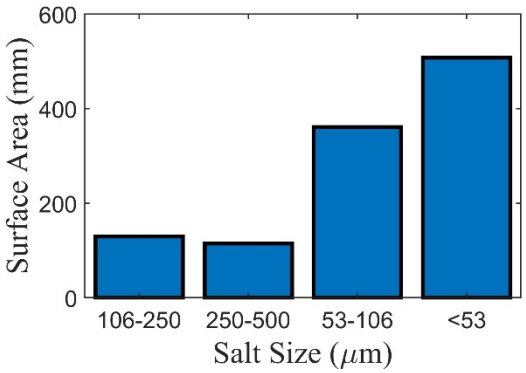

Figure 14: Comparison of open-cell pore surface area for the four PVDF samples examined

4.0 Conclusion

μ-CT can be used as a powerful and non-destructive characterization method for obtaining a 3D digital model from the pore structure of open cellular PVDF foam. The methods outlined to give a detailed approach to the usage of μ-CT to quantify fundamental morphological properties digitally. Scans of the PVDF sample were taken at a resolution of 4904x3280 pixels at a pixel size of 0.8 μm. The total geometric volume of the sample was then found by digitally filling the pores in the foamed sample and subtracting a filled-in sample from the original sample images. By doing, so both the volume and surface area of the pores was determined. This information was then used to study the porosity of the sample and the total surface area of them. Finally, by digitally eroding the samples, the individual pores can be defined from the pore network.

The porosity values obtained in this study were found by calculating the ratio of the total geometric volume to open cell pore network volume in voxels. The porosity was found to lay between 60.38%-69.28% for the four samples. Disregarding the <53 μm sample, which had a substantially smaller porosity than the other samples, the measured porosity was between 67.51%-69.28%, which closely relates to the expected 70% porosity. The unexpectedly low porosity value for the <53μm sample was likely a result of an uneven dispersion of salts within the polymer during the manufacturing process. Results for the 250-500 μm, 105-250 μm, and 53-106 μm samples were plotted to examine the effect of salt size on their distribution within each sample. The results confirmed that the distribution of pore sizes corresponded to the used salt particle size and that smaller salt sizes result in greater pore overlap.

When trying to analyze the constituent salts sizes digitally, all samples seemed to show a behaviour that was biased towards the smaller pore sizes. This behaviour is expected as the erosion process preformed to separate the samples. A second variation in the 53-106 μm sample was the

presence of some large pores well beyond the 106 μm range that contributed to about 16% of the total pore value. Overestimation of pore volume was likely due to the significant overlapping between the salts within the sample, which makes it hard to separate the pores properly. Finally, the surface area of porous samples was investigated. The relation of the particle size showed a nonlinear increase in surface area as the pore sizes became small. These results have shown a strong promise for the ability of CT analysis and digital image techniques to accurately characterize the essential details of the microstructure for a polymer foam. The methods outlined in this work have the potential for use as a post-manufacturing technique to help identify any inconsistencies in materials and limitations within the manufacturing process.

5.0 References

[1] P. Bai *et al.*, "Dipole-moment-induced effect on contact electrification for triboelectric nanogenerators," vol. 7, no. 7, pp. 990–997, 2014.

[2] K. Y. Lee *et al.*, "Hydrophobic sponge structure-based triboelectric nanogenerator," *Adv. Mater.*, vol. 26, no. 29, pp. 5037–5042, 2014.

[3] E. Fukada, "History and Recent Progress in," *Ieee Transduct. Ultrason. Freq. Control*, vol. 47, no. 6, pp. 1277–1289, 2000.

[4] Y. Xin *et al.*, "PVDF tactile sensors for detecting contact force and slip: A review," *Ferroelectrics*, 2016.

[5] B. S. Kim, M. K. Lee, and J. Lee, "Large-area PVDF membranes with through-thickness porosity prepared by uni-directional freezing," *Macromol. Res.*, 2013.

[6] M. Hossein Razzaghi, A. Safekordi, M. Tavakolmoghadam, F. Rekabdar, and M. Hemmati, "Morphological and separation performance study of PVDF/CA blend membranes," *J. Memb. Sci.*, 2014.

[7] Y. Bian, R. Liu, X. Huang, J. Hong, H. Huang, and S. Hui, "Design and fabrication of a metal core PVDF fiber for an air flow sensor," *Smart Mater. Struct.*, 2015.

[8] S. K. Boyd, "Micro-computed tomography," in *Advanced Imaging in Biology and Medicine: Technology, Software Environments, Applications*, 2009.

[9] L. P. Djukic, I. Herszberg, W. R. Walsh, G. A. Schoeppner, B. Gangadhara Prusty, and D. W. Kelly, "Contrast enhancement in visualisation of woven composite tow architecture using a MicroCT Scanner. Part 1: Fabric coating and resin additives," *Compos. Part A Appl. Sci. Manuf.*, 2009.

[10] L. P. Djukic, I. Herszberg, W. R. Walsh, G. A. Schoeppner, and B. Gangadhara Prusty, "Contrast enhancement in visualisation of woven composite architecture using a MicroCT Scanner. Part 2: Tow and preform coatings," *Compos. Part A Appl. Sci. Manuf.*, 2009.

[11] V. Cnudde, A. Cwirzen, B. Masschaele, and P. J. S. Jacobs, "Porosity and microstructure characterization of building stones and concretes," *Eng. Geol.*, 2009.

[12] V. Cnudde, M. Boone, J. Dewanckele, M. Dierick, L. Van Hoorebeke, and P. Jacobs, "3D characterization of sandstone by means of X-ray computed tomography," *Geosphere*, 2011.

[13] Skarzyński and J. Tejchman, “Experimental investigations of fracture process in concrete by means of X-ray micro-computed tomography,” *Strain*, 2016.

[14] X. Cai, A. A. Malcolm, B. S. Wong, and Z. Fan, “Measurement and characterization of porosity in aluminium selective laser melting parts using X-ray CT,” *Virtual Phys. Prototyp.*, 2015.

[15] F. Desplentere, S. V. Lomov, D. L. Woerdeman, I. Verpoest, M. Wevers, and A. Bogdanovich, “Micro-CT characterization of variability in 3D textile architecture,” *Compos. Sci. Technol.*, 2005.

[16] J. E. Little, X. Yuan, and M. I. Jones, “Characterisation of voids in fibre reinforced composite materials,” *NDT E Int.*, 2012.

[17] G. W. Melenka, E. Lepp, B. K. O. Cheung, and J. P. Carey, “Micro-computed tomography analysis of tubular braided composites,” *Compos. Struct.*, 2015.

[18] J. Ya, Z. Liu, and Y. Wang, “Micro-CT Characterization on the Meso-Structure of Three-Dimensional Full Five-Directional Braided Composite,” *Appl. Compos. Mater.*, 2017.

[19] R. K. M. Chu, H. E. Naguib, and N. Atalla, “Synthesis and characterization of open-cell foams forsound absorption with rotational molding method,” *Polym. Eng. Sci.*, 2009.

[20] S. Ghosh *et al.*, “Dynamic mechanical behavior of starch-based scaffolds in dry and physiologically simulated conditions: Effect of porosity and pore size,” *Acta Biomater.*, 2008.

[21] M. Du Plessis, “Relationship between specific surface area and pore dimension of high porosity nanoporous silicon - Model and experiment,” *Phys. Status Solidi Appl. Mater. Sci.*, 2007.